Deposition of Aluminum-Doped ZnO Films by ICP Assisted Sputtering

Yoshinobu Matsuda[1], Akinori Hirashima[2], Kenji Mine[2], Takuhiro Hashimoto[1], Daichi Matsuoka[1], and Masanori Shinohara[1], and Tatsuo Okada[3]

[1] *Graduate School of Engineering, Nagasaki University, Bunkyo 1-14, Nagasaki 852-8131, Japan.*

[2] *Graduate School of Sci. & Technology, Nagasaki University, Bunkyo 1-14 Nagasaki 852-8131, Japan.*

[3] *Graduate School of Information Science and Electrical Engineering, Kyushu University, Fukuoka 812-8581, Japan.*

ymat@nagasaki-u.ac.jp

Abstract

Inductively coupled plasma (ICP) assisted DC sputter-deposition was used for the deposition of Al-doped ZnO (AZO or ZnO:Al) thin films. With increasing ICP RF power, film properties including deposition rate, crystallinity, transparency and resistivity were improved. To understand the plasma-surface interaction, several plasma diagnostics were performed. Heat fluxes to the substrate were measured by thermal probes, number densities of sputtered metallic atom species were measured by absorption spectroscopy using hollow cathode lamps (HCL) and light emitting diodes (LEDs), and neutral gas temperatures were measured by external cavity diode laser (ECDL) absorption spectroscopy. As a result, it was revealed that the high density ICP heated the substrate through a high heat flux to the substrate, resulting in a high quality film deposition without the need for intentional substrate heating. The heat flux to the substrate was predominantly contributed by the plasma charged species, not by the neutral Ar atoms which were also significantly heated in the ICP. The substrate position where the highest quality films were obtained was found to coincide with the position where the substrate heat flux took the maximum value.

1. Introduction

Transparent conductive oxide (TCO) thin films with high transparency in the visible and near infrared spectral region and low resistivity [1,2] have been widely used as transparent conducting electrodes for various optoelectronic devices such as solar cells, flat panel displays, etc. Some TCO materials such as SnO_2 and In_2O_3 have already been put to practical use in industry. In particular, Sn-doped In_2O_3 (ITO) has been widely used so far due to its high transparency in the visible region, high chemical stability and low resistivity. Metal-doped ZnO which first appeared around 1980 has recently received attention as one of the alternatives to the ITO. Doped ZnO thin films with In (IZO), Ga (GZO) and/or Al(AZO) have high carrier densities of $10^{20}\sim10^{21}cm^{-3}$ and low electric resistivity of $10^{-2}\sim10^{-4}$ Ωcm. The origin of conductivity, nonstoichiometry and coloration for TCOs has recently been gradually understood [3-5]. We focus here AZO thin films, since the AZO has advantages over ITO and other doped ZnO in environment resistance and resource cost. To actually replace the ITO with the AZO, however, reproducible and highly-reliable fabrication processes of good quality polycrystalline AZO thin films have to be developed.

The polycrystalline AZO films have been prepared by a variety of techniques such as reactive and nonreactive magnetron sputtering [6], high density plasma assisted (or superimposed) magnetron sputtering [7-12], chemical vapor deposition [13], pulsed-laser deposition [14], evaporation [15], spray-pyrolysis [16], Sol-gel preparation [17] and electrochemical deposition [18]. Among them, magnetron sputtering is one of the dominant deposition techniques for the deposition of good quality, large area coating with relatively low substrate temperature [6].

High density inductively coupled plasma (ICP) assisted magnetron sputtering [19-23] is also a promising technique because it requires no intentional substrate heating due to high plasma density. The advantages of ICP-assisted sputtering are summarized as follows: 1) the target is sputtered with low target voltage and high target current, 2) the usage efficiency of the target is significantly improved due to the

expansion of erosion area, 3) ionization and excitation of the sputtered particles are enhanced in the ICP and the enhanced ion fluxes to the substrate promote the crystallinity of thin films without intentional substrate heating, 4) lateral homogeneity of the deposited film is greatly improved, and 5) abnormal discharge (arcing) [24,25] is drastically suppressed . However, previous research showed the lowest resistivity of AZO films prepared by the ICP assisted sputtering is limited around 10^{-3} Ωcm [9-12]. To understand the ICP assisted sputter-deposition mechanism and to improve the AZO film quality, we have investigated AZO film deposition process by using ICP assisted DC magnetron sputtering [26-30].

This paper summarizes the experimental results on the basic discharge characteristics, heat flux to the substrate, sputtered atom densities and the neutral gas temperatures in the bulk plasma, and the film properties (deposition rate, resistivity, transparency, crystallinity, and elemental ratio) of prepared AZO films in the ICP assisted sputter-deposition process. The effect of ICP superimposing on the bulk plasma and the film properties is discussed.

2. Experimental Setup and Procedure of ICP assisted Magnetron Sputtering

Figure 1 shows the experimental setup for the ICP sputter-deposition of Al doped ZnO thin films [26-30]. A 3 inch DC planar magnetron, an Ar gas supply system and a pumping system (turbo molecular pump and rotary pump combination) were attached to the vacuum chamber (300 mm in diameter and 300mm in height). After the base pressure of around 10^{-6} Torr was attained, Ar was introduced by a mass flow controller. Then, the working pressure was set at 4 Pa by tuning the conductance of the main valve. A disk target of ZnO: Al_2O_3 (2 wt%) of 60 mm diameter and 6mm thick was used as a target, and a glass substrate was set on an earthed substrate holder with a gap length of 80mm. Between the target and the substrate, a single turn coil antenna of 100 mm diameter was installed and used for producing 13.56 MHz ICP. The antenna was covered with insulator and water-cooled. The distance from the target to the RF coil (T-C distance) and the distance from the RF coil to the substrate (C-S distance) were both 40 mm. The

magnetron plasma was generated by applying negative DC voltage to the target electrode, and the ICP was generated by applying 13.56 MHz RF power to the coil antenna through a matching circuit. After the thin film deposition, the substrate was taken out from the vacuum chamber and cut to several pieces. Characteristic of each thin film (film thickness, resistivity, transmission, crystallinity, and elemental ratio) and their lateral distribution on the substrate were evaluated.

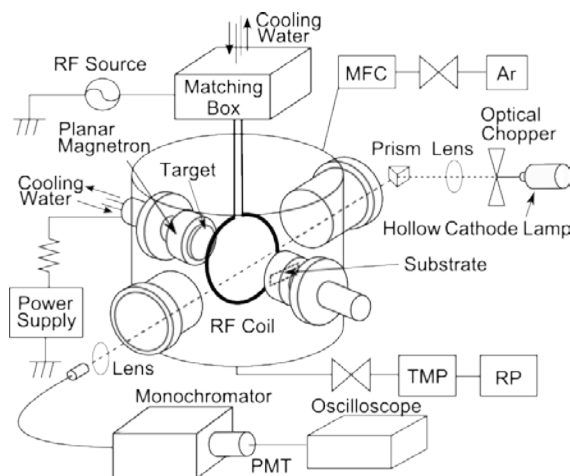

Fig. 1 Experimental Setup for ICP assisted DC magnetron sputter-deposition and for hollow cathode absorption measurement.

The film thickness was measured by a stylus-profile meter (Mitsutoyo, SV-400). The electric conductivity was measured by a four point probe and the film resistivity was evaluated by multiplying the experimental surface resistance by a geometrical correction factor determined by the film thickness, substrate shape and size and distance between the probe tips. The optical transmission was measured by a spectral photometer consisting of a halogen lamp and an optical fiber-spectrometer (Ocean Optics, HR4000CG). In this work, we evaluated the optical transmittance of AZO films by using “the overall transmittance” that was averaged over visible wavelength range (380-780 nm) and further averaged over lateral spatial distribution. However, since the overall transmittance mentioned above depends on the film thickness, we judged the optical property utilizing the absorption coefficient α (absorbance per unit thickness) by $\alpha = \ln(1/T)/d$, where T is the overall averaged transmittance, d is the film thickness. For

example, let d =300 nm and $T = 90$ %; it gives $\alpha = 0.4$ μm^{-1}. The crystallinity of thin films was investigated by X-ray diffraction (RINGAKU, RINT2000). The elemental ratio in the film was measured by X-ray photoemission spectroscopy (SHIMADZU-KRATOS, AXIS-HS). Details of the plasma diagnostics will be explained in the section 4.

3. ICP Assisted Sputter-Deposition of Aluminum Doped Zinc Oxide Thin Films

3.1. Influence of Distance between Target, ICP Coil, and Substrate on Film Properties

First, the optimum geometry conditions concerning (a) target voltage, (b) target current, (c) deposition rate, (d) resistivity, and (e) transmittance were investigated by varying the T-C distance from 10 to 50 mm and the C-S distance from 30 to 70 mm, respectively. Figure 2 shows the results of the investigation for the condition of 4 Pa Ar discharges with a DC target power of 40 W and ICP-RF power of 200 W. As can be seen from (a) and (b) in Fig.2, the target voltage decreases and the target current increases with increasing T-C distance; i.e., the impedance of the discharge increases with increasing the gap length between the target and the ICP coil. This is predominantly explained by the fact that the diffusion loss of charged particles in the plasma is enhanced by decreasing the T-C distance because the ground shield of the magnetron target works as a sink of plasma particles. The T-C distance dependence of the target discharge impedance shown in Fig. 2 (a) and (b) does not hold for the larger T-C distances. For the larger T-C distances, the target discharge impedance will decrease and get closer to that for the planar magnetron discharge because the magnetron plasma is isolated from the ICP. The C-S distance dependence of the target voltage and the target current is minimal compared with the T-C distance dependence. From a view point of thin film deposition, low discharge impedance is favorable because of low bombarding damage of the films. Thus, longer T-C and C-S are favorable. As can be seen from Fig.2 (c), however, the deposition rate decreases with increasing T-C and C-S distances, i.e., the deposition rate and the discharge impedance have a “trade-off” relationship. In addition, we can see there is a trade-off

between the film resistivity and the transmittance. Thus, as a result of compromise between the trade-offs, we determined the optimal values for both the T-C distance and the C-S distance to be 4 cm. We confirmed that the AZO film with a resistivity of 2×10^{-3} Ωcm and a transmittance of more than 80 % can be obtained with good reproducibility under this condition at ICP-RF power of 200-300 W.

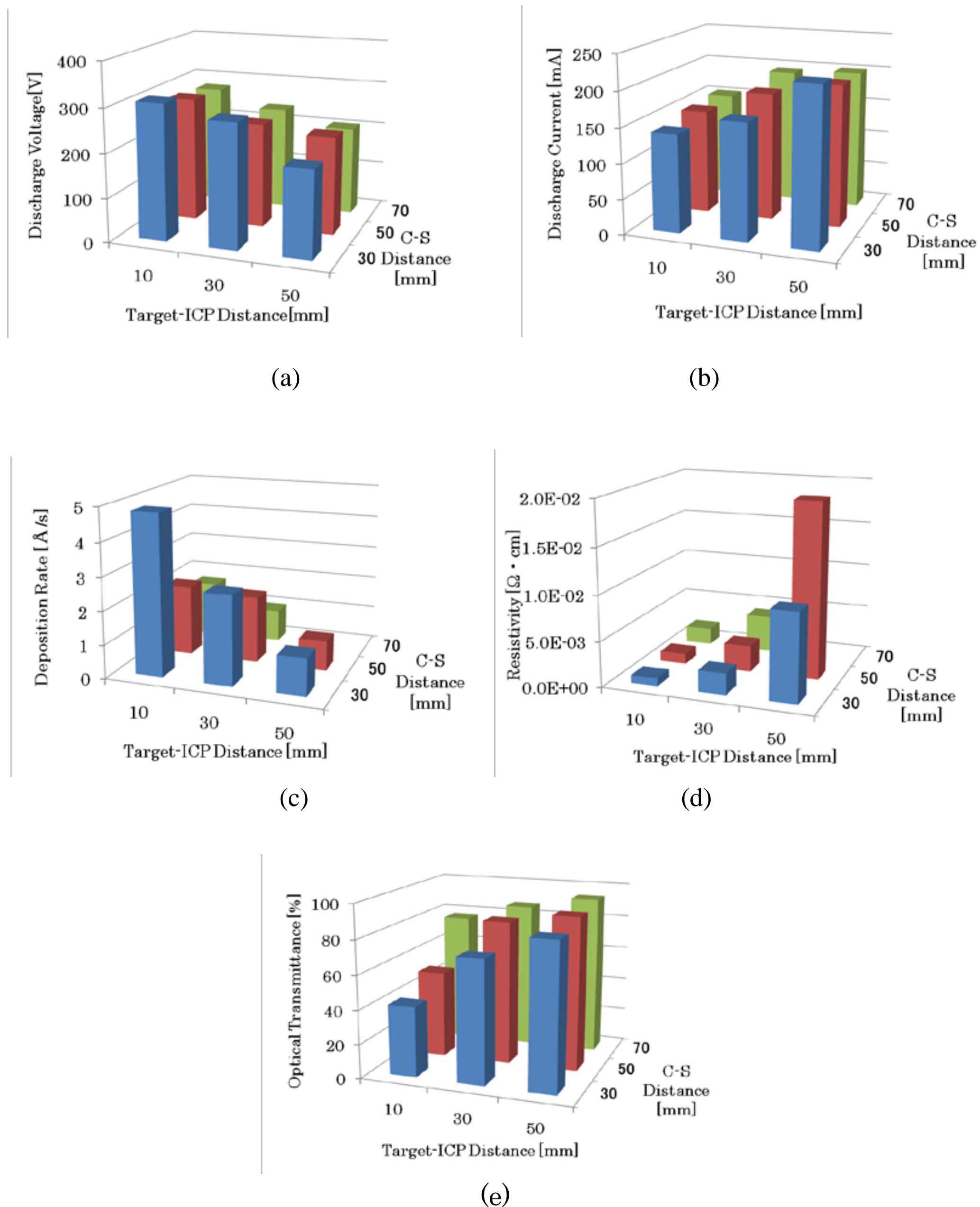

Fig. 2 (a) Target voltage, (b) target current, (c) deposition rate, (d) resistivity, and (e) transmittance against the target-ICP coil distance and the ICP-coil and Substrate distance.

3.2. Effect of ICP-RF Assist Power

Figure 3 shows the ICP RF power dependence of the target discharge voltage and the target discharge current for the constant target input power at 45 W. The target discharge voltage decreases and the discharge current increases with increasing ICP RF power. Therefore, the impedance for the sputtering discharge decreases with the increase in ICP RF power. This is because the plasma density near the planar magnetron target is increased by the presence of ICP, whose density almost increases linearly with the ICP RF power. The decrease in the target discharge impedance under the ICP assisted sputtering is extremely effective because the low voltage sputtering is directly connected to the reduction of film damage on the substrate. Moreover, the low voltage sputtering is very effective for suppressing arcing. ICP assisted sputtering is effective for the improvement in the usage efficiency of the target and the uniformity of thin film characteristics because the sputtering area expands to the whole target surface.

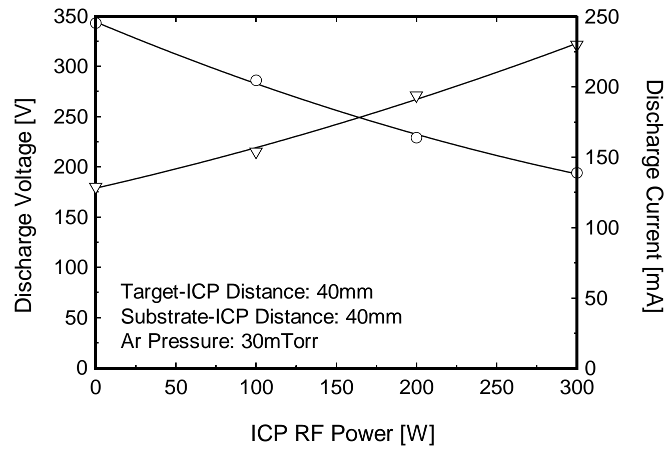

Fig. 3 ICP RF power dependence of discharge voltage (circle) and discharge current (triangle) during ICP assist magnetron sputtering at the working pressure of 4 Pa and at a constant target power of 45 W.

The change in the plasma emission intensity with and without ICP superimposing was investigated. It was found that predominant optical emission lines are only due to the electron impact excitation of sputtered Zn atoms within the wavelength range from 200 to 400 nm without ICP assist. In the case of ICP

assisted magnetron discharges, optical emission intensities for the Zn I lines are significantly increased, and additional optical emission lines from much higher excited states of Zn atoms and from excited states of Al atoms were identified. Thus, the ICP assisted sputter-deposition with promoted excitation and ionization is effective for enhancing the crystallinity of deposited AZO films.

Figure 4 shows the ICP RF power dependence of the spatial distribution of deposition rate. It is found that the deposition rate increases by 20-30 % with increasing ICP RF power from 0 to 300 W. This tendency can be explained by the increased sputtered particle flux due to self sputtering effect. With increasing ICP RF power, ionized degree of sputtered Al and Zn atoms is increased and the Al and Zn ions bombard the target as well as the substrate, resulting in self sputtering that enhances the sputtered flux. However, since the increase in the deposition rate with increasing ICP RF power is much smaller than that of sputtered Zn atom density that will be described in the section 4.2, we can consider that a re-evaporation of Zn atoms from the substrate likely occurred during the deposition process.

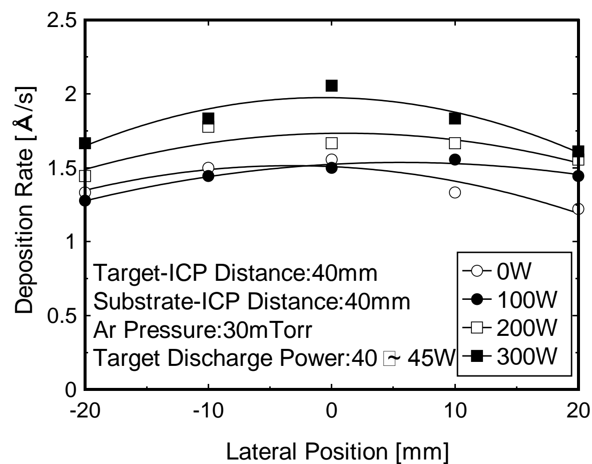

Fig. 4 ICP RF power dependence of deposition rate of AZO thin films.

Figure 5 shows the ICP RF power dependence of the spatial distribution of film resistivity. The resistivity is very high about 2×10^{-1} Ωcm for the planar magnetron discharge without ICP at the pressure 4 Pa. However, the resistivity is drastically decreased and the uniformity is improved with increasing ICP RF

power. It is well known that for DC magnetron sputtering operating at below 1 Pa the resistivity of the film is comparatively low at both the center and peripheries, while the resistivity is high at the substrate positions facing the target erosion However, in the ICP assisted sputtering with operating pressures at around 4 Pa, the spatial profile of resistivity is more uniform. The drastic decrease in the resistivity due to the ICP assist is explained as follows. When the ICP RF power increases, the film damage decreases because the target voltage decreases, and the energies of charged and neutral species incident to the substrate decrease. In addition to this effect, total ion flux to the substrate with moderate energies of about 10-20 electron volts increases due to the increase in plasma density with increasing ICP RF power. The increased energy flux to the substrate heats the substrate surface up to a temperature around 200 ºC or more and the film crystallinity is improved. In this research, conductive AZO films with resistivity of 2×10^{-3} Ωcm were obtained with good spatial uniformity. Hall measurement result showed the carrier density and carrier mobility were typically 5×10^{20} cm^{-3} and 6-7 $cm^2/(Vs)$ for the AZO films deposited at ICP RF power of 300 W. To decrease more the resistivity of AZO films deposited in this scheme, further increase in the mobility is needed.

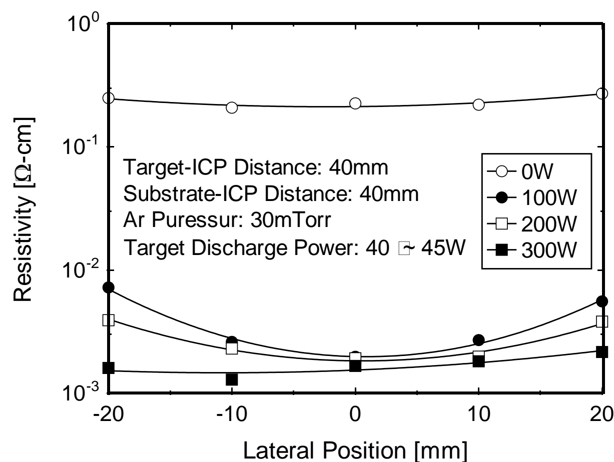

Fig. 5 ICP RF power dependence of resistivity of AZO thin films.

Assisting ICP RF power is effective for increasing film transparency. Figure 6 shows the ICP RF power dependence of the absorption coefficient of deposited AZO films. The vertical axis of Fig. 6 is the averaged absorption coefficient α as explained in the Section 2. We judged the films with absorption coefficients less than 0.5 μm^{-1} have excellent optical transparency. Though the optical transmittance of deposited films is satisfactory for any ICP RF power, the transparency is much improved for ICP RF power more than 100 W as is shown in Fig. 6.

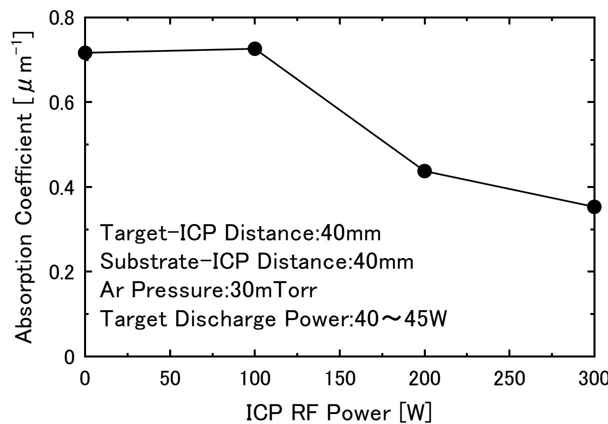

Fig. 6 ICP RF power dependence of averaged absorption coefficient of AZO thin films.

Figure 7 shows the change in the X-ray diffraction pattern of AZO films with the same thickness of about 300 nm obtained at 5.33 Pa for the ICP RF power of 0, 100, 200, and 300W. The strong (002) diffraction peak indicates that the films are highly texturized with the c-axis perpendicular to the substrate surface, which is well known structure for good quality polycrystalline ZnO [3]. The intensity and the width of this peak indicate the fraction of crystallization and the grain size. From Fig.7, we find that the intensity of (002) peak is enhanced with increasing ICP RF power, but the grain size depends weakly on the ICP RF power. The crystallinity of film is promoted with increasing ICP RF power, since the sputtered particles are more excited and ionized and ion fluxes to the substrate are increased in the ICP, resulting in the elevation of substrate surface temperature. However, the number of initial nucleation is already determined at the early deposition stage, resulting in a weak ICP RF power dependence of the grain size. It

suggests that the control of initial nucleation density is important to get large grain sizes that will be effective for increasing carrier mobility.

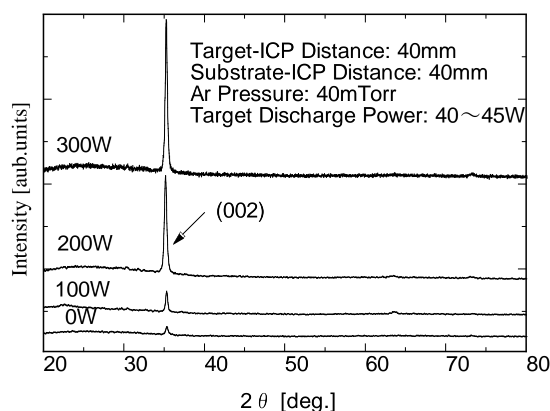

Fig. 7 ICP-RF power dependence of X-ray diffraction pattern.

Figure 8 shows the ICP RF power dependence of the elemental ratio of Al and resistivity in the AZO films. The elemental ratio of Al was obtained from the XPS analysis of Al 2p signal. With increasing ICP RF power, the elemental ratio of Al in the film increases and the resistivity decreases. Since the ZnO: Al_2O_3 (2 wt%) target contained 1.56 at % Al, it is found that the fraction of Al in the deposited AZO films changed depending on the ICP RF power. The ICP RF power dependence of the elemental ratio of Al in the film is in agreement with the ICP RF power dependence of the relative gas phase density of Al to Zn atoms. This will be shown in the later section 4.2, which is understood by a large evaporation pressure of Zn. The carrier density of AZO depends on the number densities of donor Al ions and O vacancies, while the carrier mobility depends on the crystallinity of thin films. Thus, it is considered that a rapid decrease in the resistivity is caused not only by the increase in carrier density due to the increase in content of Al atom, but also by the increases in the number density of O vacancies and carrier mobility due to the promotion of crystallinity of thin film as shown in Fig. 8. We have also investigated on an AZO target containing 4 wt% Al_2O_3 (or 3.1 at% Al), but the resistivity of AZO (4 wt% Al_2O_3) was several times larger than that of AZO

(2 wt% Al_2O_3) for the same ICP RF power range. It is reported that the excess Al fraction in the film causes a decrease in mobility possibly due to the increase in ionized impurity scattering [3].

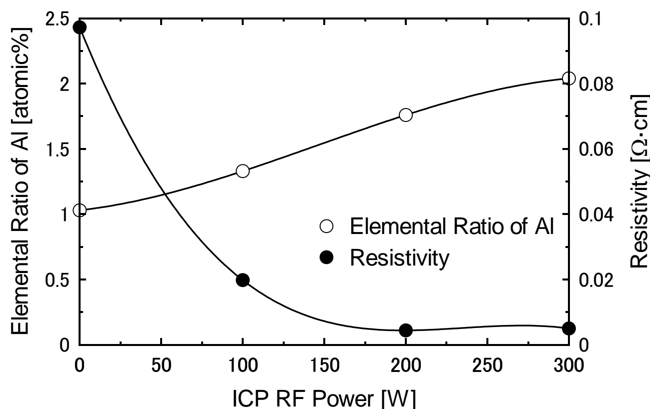

Fig. 8 ICP RF power dependence of elemental ratio of Al in the film and resistivity.

3.3. Effect of Hydrogen Addition

In conventional RF sputtering, it is well known that the electric conductivity of the AZO film is increased when hydrogen gas is added to Ar [31]. Thus, we have investigated the effect of hydrogen addition on the electric conductivity, optical transmittance, and deposition rate of the AZO thin films deposited by ICP assisted sputter-deposition. A small amount of hydrogen was mixed with Ar and the total gas pressure was fixed at 4 Pa. The amount of hydrogen addition was changed by setting the preset partial pressure of hydrogen before each deposition. The fraction of hydrogen defined by C_H (= $[H_2]/([Ar]+[H_2])$) was varied in steps 0, 0.25, 0.5 and 1 %. The ultimate pressure in the chamber was 3×10^{-6} Torr or less. The flow rate of Ar was adjusted to 50sccm. The sputtering power (target power) and the ICP RF power were fixed at 44 W and 200 W, respectively. Deposition time was 30 minutes for all samples.

Figures 9 and 10 show the change in resistivity, transmittance and deposition rate of ZnO films against the hydrogen mixture fraction. From Fig.9, it is found that the film conductivity is slightly improved; the minimum resistivity of 1.8×10^{-3} Ω cm was obtained at C_H=0.25 %. Excess addition of hydrogen over than 0.5 %, however, decreased the film conductivity. The decrease in film resistivity at C_H=0.25 % is

explained by the increase in the carrier density, i.e., free electron density due to the increased production of oxygen vacancy. On the other hand, the increase in film resistivity at C_H=0.5 and 1.0 % is explained by the decrease in the carrier mobility due to the degraded crystallinity owing to the excess subtraction of oxygen atoms by the hydrogen atoms. The dependence of the resistivity on hydrogen mixture ratio directly correlates with those of the transmittance and the deposition rate shown in Fig. 9. A drastic decrease in the optical transmittance and the deposition rate at C_H=1.0 % is considered to be due to the influence of the excess hydrogen atom density in the AZO thin films as well as in the plasma.

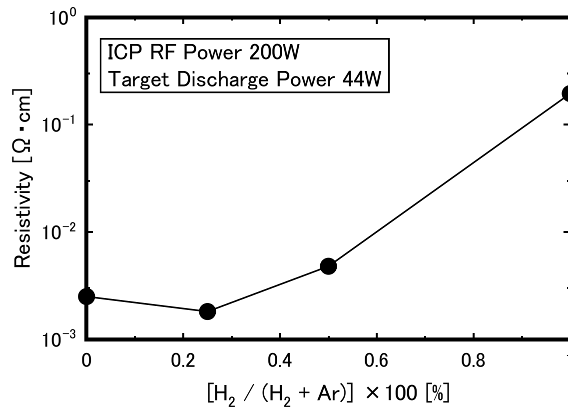

Fig. 9 Hydrogen mixture ratio dependence of resistivity of AZO films .

It is reported that the lowest resistivity of 2.8×10^{-4} Ω cm, which is a half or a thirds of the value without hydrogen addition, was obtained when the partial pressure ratio of hydrogen is C_H = 10 % [31]. In Ref. 31, a conventional 4 inch RF magnetron was used and the optimum working pressure and RF power were 0.4 Pa and 100 W. However, our experimental condition is very different from that of Ref. 31 in that the sputter-deposition was done at much higher pressure around 4 Pa, with lower sputtering power and with additional ICP RF power of 200W. In the ICP, hydrogen molecules are efficiently dissociated and the flux ratio of atomic hydrogen atoms to the sputter-deposited species would be much higher compared with the CCP case of Ref. 31. This is the reason why the effect of hydrogen addition appeared at much smaller amount of hydrogen addition than that reported in Ref. 31.

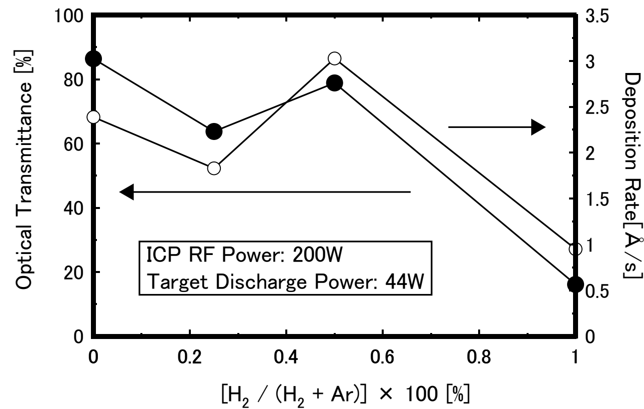

Fig. 10 Hydrogen mixture ratio dependence of optical transmittance and deposition rate of AZO films.

4. Diagnostics of ICP Assisted Sputter-Deposition Processes

As mentioned in the Section 3. 2, crystallization with high orientation along (002) is promoted without intentional substrate heating in the ICP assisted sputter-deposition with increasing ICP RF power. To understand the sputter-deposition mechanism and to improve the film quality further, it is important to reveal the reactions in the gas phase and on the surface. Thus, we have developed several plasma diagnostic systems and applied them as follows: (4.1) heat flux measurement by home-made thermal probes (TPs), (4.2) density measurement of sputtered Al and Zn atoms by absorption spectroscopy with hollow cathode lamps (HCLs) and LEDs, and (4.3) gas temperature measurement by absorption spectroscopy with a tunable external cavity diode laser (ECDL). These are explained below.

4.1. Measurement of Spatial Distribution of Heat Flux to the Substrate

Energy flux to a substrate was measured by many researchers using variety of thermal probes (TPs) in the past in the RF plasma [32-37], RF magnetron plasma [38, 39], and DC grow discharge plasma [40]. However, no measurement of the energy flux to the substrate during the ICP assisted sputtering has been done to our knowledge. Thus, we have made several TPs with the help of many references [32-40] to grasp the energy flux onto a substrate during the ICP assisted sputtering.

The energy flux (energy per unit area per second) J to a substrate can be measured with a TP via two

different ways: steady state operation or pulse operation depending on the “plasma on” time duration. In the steady state operation, plasma is turned on much longer than the thermal relaxation time of the TP, and the temperature gradient ($\Delta T/\Delta x$) on the TP is measured after the TP is thermally equilibrated. Then, the equilibrium J is simply evaluated by the equation

$$J = -k\frac{\Delta T}{\Delta x} \quad , \qquad (1)$$

where k[W/(m·K)] is thermal conductivity. Thus, absolute value of J is measured, even though it takes a long time. Conversely, in the case of the pulse operation, plasma is turned on in a short period of time (shorter than the thermal time constant) and then turned off. From a transient change of the probe tip temperature, J is evaluated by the following equation [32-35]:

$$J = \frac{mc}{S}\left[\left(\frac{dT_s}{dt}\right)_{\mathrm{on}} - \left(\frac{dT_s}{dt}\right)_{\mathrm{off}}\right]_{T_S} \quad , \qquad (2)$$

where mc is the thermal capacity (m: mass of probe head, c: specific heat), S is the probe surface area, and $[(dT_s/\mathrm{d}t)_{\mathrm{on}}-(dT_s/\mathrm{d}t)_{\mathrm{off}}]$ is the difference in temperature gradient at common substrate temperature T_s during heating and cooling period.

4.1.1. Development of a thermal probe for absolute energy flux measurement [41-43]

Figure 11 shows a schematic of a TP made in this work. The TP is composed of a Cu plate (10 mm in diameter, 0.1 mm in thickness) facing to the plasma, a ceramics rod (6 mm in diameter, 10 mm in length) producing temperature gradient, an Al rod (6 mm in diameter, 350 mm in length) connected to the outer heat sink, and outer tubes (Teflon and stainless steel tubes) for thermal and electric insulation, which prevents the energy flux from coming in from the side of the TP. The Cu plate, ceramic rod and Al rod were tightly bonded. The first thermocouple was attached to the ceramic rod at the distance of 6mm from the joint plane between the ceramic and the Al rod, and the second thermocouple was attached on the Al rod with a distance of 10mm from the joint plane. The other end of the Al rod was water-cooled outside the vacuum vessel. The outer stainless steel tube for heat insulation was grounded to cut the electrical coupling between the TP and plasmas. The greatest thermal gradient appears on the ceramic rod that has a

thermal conductivity of 1.6 W/(m･K). The length of the ceramics rod was determined by the tradeoff between the requirements of a smaller thermal time constant of the ceramic rod and a larger temperature difference at the both ends of the ceramic rod. The thermal time constant is expressed as follows:

$$\tau = CR = \rho\, cV \frac{L}{kS} = \frac{\rho\, c}{k} L^2 \quad , \qquad (3)$$

where C is thermal capacity, R is thermal resistance, ρ[kg/m^3] is mass density, c [J/(kg･K)] is specific heat, k[W/(m･K)] is thermal conductivity, V [m^3] is volume, S [m^2] is cross section area, L [m] is length of the TP body. The shorter the length of ceramic rod, the smaller the thermal time constant. The copper plate of TP was biased by connecting a lead wire. As a result of investigation of the influence of film deposition on probe surface, we confirmed that the measured value decreased 4 % by a film deposition thickness of 100 nm. To clean the copper plate surface, the bias voltage of -100V was applied for fifteen minutes before each experiment.

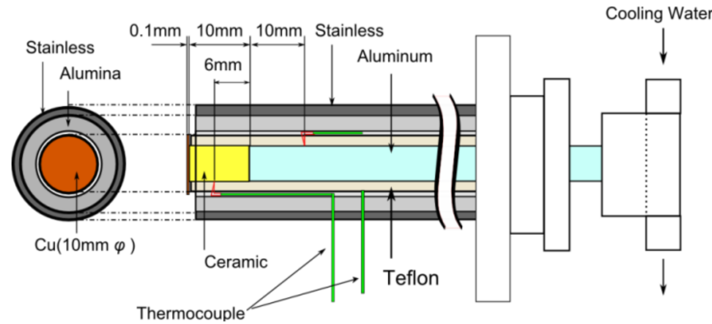

Fig. 11 Schematic of a TP for the absolute heat flux measurement.

The TP was set 8 cm from the target surface in the axial direction, and 3 cm from the center axis of magnetron. Figure 12 shows a temporal change of difference in temperature measured by the two thermocouples on the TP for the ICP RF power 100 and 200 W when plasma on period was 60 s (pulse operation) and 700 s (steady state operation). The data shown in Fig. 12 indicates that the difference in temperature is mostly saturated with a time constant τ of 160 s and the thermal equilibrium condition is reached at the time after 3-4 τ seconds. In the steady state operation, the energy flux was evaluated by eq. (1), however it should be considered that the time interval between each measurement took about 1-2 hours because the heating time of 3-4 τ and the cooling time of several tens of τ were required. In the

pulse operation, the energy flux was estimated by eq. (2) by calibrating *mc/S* with the absolute value of energy flux measured in the steady state operation. Thus, the time interval between each measurement was reduced by one order of magnitude.

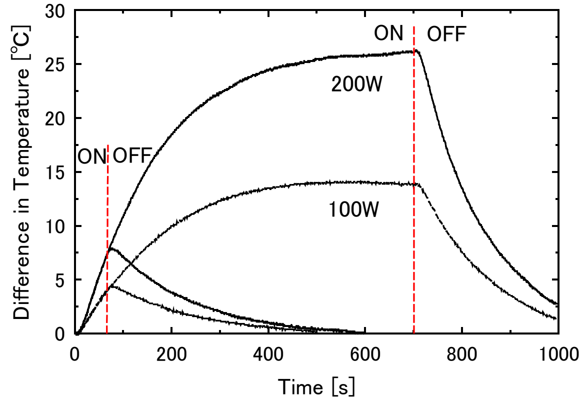

Fig. 12 Temporal change in temperature difference obtained by a thermal probe during plasma on and off period for ICP RF power of 100 and 200 W.

To evaluate the validity of the energy flux measurement in the pulse operation, we compared the variation of the term $[(dT_s/dt)_{on}-(dT_s/dt)_{off}]$ against common substrate temperature difference T_s. As a result, it was found that the term $[(dT_s/dt)_{on}-(dT_s/dt)_{off}]$ in eq, (2) was almost constant within the error of ±5% when the T_s was taken in the range of 30~100% of the maximum temperature difference. Thus, the *mc/S* of the TP was correctly calibrated by dividing the absolute energy flux measured at the same sampling point in the steady state operation by the constant value of $[(dT_s/dt)_{on}-(dT_s/dt)_{off}]$.

Figure 13 shows ICP RF power dependence of energy flux for different target (sputtering) power of 0 W (only ICP discharge) and 40 W (ICP assisted magnetron discharge). The energy flux to the TP for the 40 W planar magnetron discharge (ICP RF power 0 W) is only 70 W/m^2. The energy flux increases with increasing ICP RF power, and it reaches 3000 W/m^2 for the ICP RF power 200 W and target power 40W. The contribution of the target (sputtering) power to the total heat flux to the substrate is less than 5 %; i.e., the energy flux in the ICP assisted sputtering is predominantly determined by the ICP RF power.

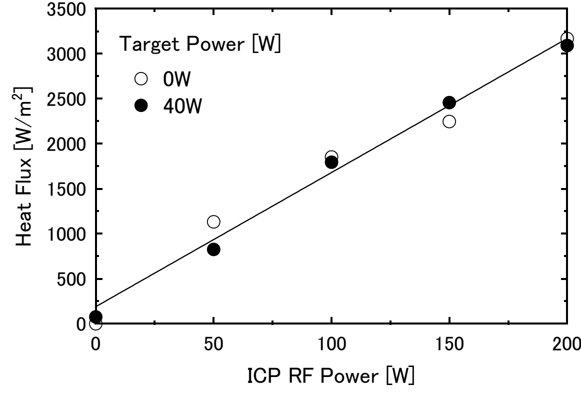

Fig. 13 ICP RF power dependence of energy flux (ICP assisted sputtering).

The change in energy flux against substrate bias was investigated experimentally and theoretically. The experimental values for the ICP RF power 200W are plotted with white circles in Fig. 14. According to Kersten et al. [35], the total energy influx to a substrate J is the sum of the fluxes due to electrons (J_e), ions (J_i), neutrals (J_n), and photons (J_p). In our case, the contributions due to the neutrals and photons were ignored because of high density ICP at 4 Pa. Thus, the total energy influx to a substrate J was simply assumed as the sum of J_i due to the kinetic energy of positive ions, J_e due to the kinetic energy of electrons, and J_{rec} due to the recombination of positive ions and electrons at the substrate surface as shown in equation (4). Here, the contribution of hot neutral species is considered to be negligible. Each contribution is expressed in eqns. (5), (6) and (7).

$$J = J_i + J_e + J_{rec} \quad , \tag{4}$$

$$J_i = j_i E_i = j_i e_0 (V_{pl} - V_s) = n_e \sqrt{\frac{kT_e}{m_i}} \exp(-0.5) e_0 (V_{pl} - V_s) , \tag{5}$$

$$J_e = n_e \sqrt{\frac{kT_e}{2\pi\, m_e}} \exp\left(-\frac{e_0 V_{bias}}{kT_e} \right) 2kT_e \quad , \tag{6}$$

$$J_{rec} = j_i E_{rec} = j_i (E_{ionization} - \phi) \quad . \tag{7}$$

Here, n_e is the electron density, kT_e the electron temperature, m_i the mass of ion, m_e the mass of electron, e_0 the base of natural logarithm, j_i the particle flux of ions, V_{pl} the plasma space potential, V_s the substrate potential, V_{bias} (= V_{pl}- V_s) the potential fall from plasma to the substrate that also equals the ion kinetic

energy E_i, E_{rec} ($=E_{ionization} - \phi$) the recombination energy of a positive ion, $E_{ionization}$ the ionization energy of Ar ions, and ϕ the work function of the substrate material.

Theoretical energy flux onto a substrate J was calculated for the pure ICP by using the experimental data on n_e, kT_e, and V_{pl}. Electron temperature, electronic density, floating potential and plasma potential were measured by a Langmuir probe respectively 2.5 eV, 2.58×10^{17} m^{-3}, 4.2 eV and 16.8 V for the condition of ICP RF power 200 W at 4 Pa. Thus, we obtained J by substituting the measured values and the physical constants such as m_e, m_i, E_{rec} (=15.7 eV for argon ion) into eqns. (5), (6), and (7). Thus, the theoretical energy fluxes of J_i, J_e, J_{rec} and the total J for 200 W ICP were calculated against V_{bias}, which are shown by colored four curves in Fig. 14. The experimental substrate bias dependence of the energy flux shown by open circles is in good agreement with the calculated total J. The result indicates that J_i, J_e, and J_{rec} dominantly contribute to the energy flux onto the substrate. It is noted that the heat flux has a minimum of 2800 W/m^2 at a floating potential of 4 V.

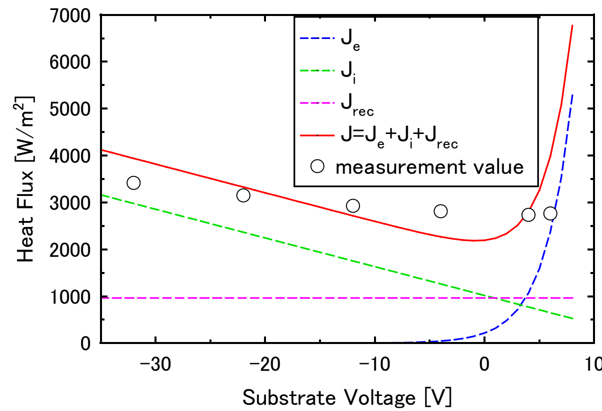

Fig. 14 Substrate bias dependence of calculated and measured energy fluxes.

4.1.2. Spatial distribution of heat flux to the substrate in ICP assisted sputter-deposition

To enable space resolved measurements of a directional energy flux in a short time, a new TP was developed. The new TP had a compact and simple structure of a small sampling Cu plate directly soldered to a small K type thermocouple wire with a stainless steel crank tube (6.35 mm diameter) behind it. The lead wire of the thermocouple was covered with alumina tubes for the radial thermal insulation in the

crank tube, and connected to a digital multi-meter to monitor temperature. The TP with crank tube was inserted from the substrate side, and the collecting electrode surface was directed to the target and ICP. Spatial distributions of directional heat fluxes were measured with the TP by rotating and transferring the crank tube. Figure 15 shows a time response of this TP during plasma on (ICP RF power 200W for 10 s) and off then after. The decay curve is composed of fast and slow components. Although the slow decay indicates that the thermal protection of the TP is imperfect, it doesn't affect the determination of the heat flux.

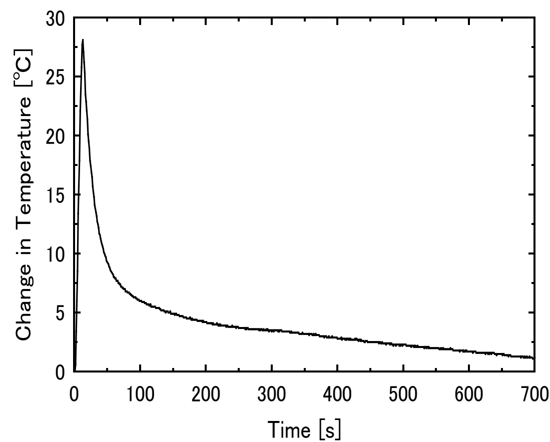

Fig. 15 Temporal change in temperature obtained by a compact thermal probe during plasma on (ICP RF power 200W for 10 s) and off.

The experimental results for the spatial profile of the directional heat flux in the ICP are shown in Fig. 16. Here, the target and ICP coil are located in the left at x=-5 and 0 cm. The Fig. 16 shows that the high heat flux region is at distances 3-5 cm from the coil, which is the same as the empirically optimized substrate positions to get high transparent and high conductive AZO films. Spatial distributions of plasma parameters such as electron density, electron temperature, plasma and floating potentials were also measured by a movable Langmuir probe. As a result, it was confirmed that the spatial profile of heat flux is similar to that of ion saturation current, and agrees rather well with the calculated heat flux profile by using these plasma parameters.

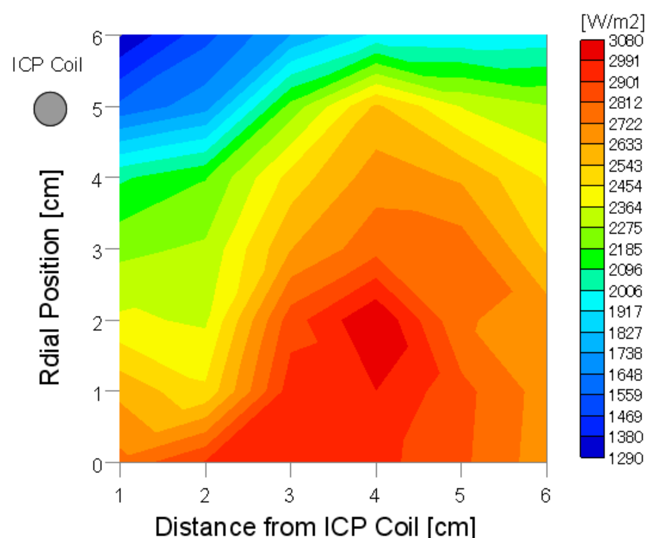

Fig.16 Spatial distribution of the directional heat flux measured by the movable TP.

4.2. Measurement of Al and Zn Atom Density Using a Hollow Cathode Lamp and UV-LEDs

The behavior of sputtered particles in the gas phase was investigated via optical emission spectroscopy and absorption spectroscopy [44]. The optical emission spectra from the excited species were monitored by employing an optical fiber spectrometer (Ocean Optics, HR4000CG-UV-NIR). For the purpose of estimating the sputtered neutral particle flux to the substrate, sputtered Al and Zn atom densities were investigated by the absorption spectroscopy using two different absorption systems: one consisting of a hollow cathode lamp (HCL)[45-49], monochromator and photomultiplier tube (HCL-M-PMT) and the other of a light emitting diode (LED) [50,51], spectrometer, and a multichannel CCD detector (LED-S-CCD).

4.2.1. Measurement of sputtered atom density with HCL-M-PMT system

Ground state densities of Al and Zn atoms sputtered from the AZO target were measured by the absorption spectroscopy using HCL-M-PMT [47-49]. Optical emission from a HCL (Hamamatsu Photonics, L233-30NQ (Zn) or L233-13NB (Al)) was passed through an optical chopper (NF, 5584A), and guided to a monochromator (JASCO, CT25) through the ICP-assisted sputtering chamber by lens,

prism and optical fiber optics. The time modulated output signal from the PMT was monitored and averaged for 1024 times on a digital oscilloscope. By comparing the difference in the modulated amplitude of PMT output between plasma ON and OFF phases, absorbance was measured. The sputtered atom density was obtained by comparing the experimental absorbance and the theoretical absorbance that was calculated using assumed gas temperatures (400K) in light source and plasma reactor and assumed optical path length (0.3m). The absorption measurements were done for Zn with 307.6 nm ($4s^2\ {}^1S_0$-$4s4p\ {}^3P_1^o$) and for Al with 396.15 nm ($3s^23p\ {}^2P_{3/2}^o$-$3s^24s\ {}^2S_{1/2}$), respectively. It is noted here that the Zn 307.6 nm line used in the experiment is a forbidden line. The use of absorption at the resonant line of Zn (213.856 nm, $4s^2\ {}^1S_0$-$4s4p\ {}^1P_1^o$) was impossible in this experiment due to too strong an absorption.

Fig. 17 shows the ICP RF power dependence of metal atom densities in gas phase. Both Zn and Al atom densities increase with increasing ICP RF power, but there is a difference in the ICP RF power dependence between Zn and Al atom densities. Al atom density linearly increases with increasing ICP RF power, while Zn atom density increases 4 times with increasing ICP RF power from 0 to 100W, then saturates for ICP RF power more than 100 W. The ICP RF power dependence of the ratio of Al to Zn density in the gas phase correlates well with that of the elemental ratio in the AZO films. The measured Al density is reliable, because the Al atom flux to the substrate was estimated $3\sim5\times10^{13}\ cm^{-2}s^{-1}$ from the measured Ar density and these values were very close to those calculated from the deposition rate of AZO. Conversely, the measured Zn density was at least two orders of magnitude greater than the expected one; i.e, the Zn atom flux of $2\sim8\times10^{17}\ cm^{-2}s^{-1}$ was deduced from the measured Zn density and the Zn atom flux of $\sim10^{15}\ cm^{-2}s^{-1}$ was estimated from the deposition rate. We have not yet identified the cause of this behavior, but we believe that it is due to the large evaporation pressure of Zn, re-evaporation of ZnO due to small formation energy compared to Al_2O_3 [52], blending of absorption by another species such as OH with Zn absorption, or another unknown factor.

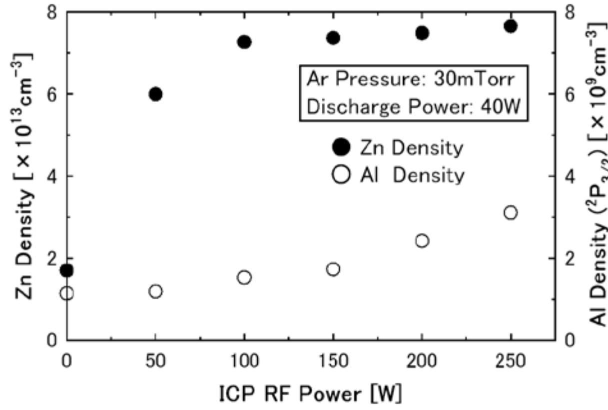

Fig. 17 ICP RF power dependence of sputtered Al and Zn atom density in front of the AZO target in ICP assisted sputtering.

4.2.2. Measurement of sputtered atom density with LED-S-CCD system [51]

Absorption measurement of Al atoms was also performed using a LED-S-CCD in a DC planar magnetron discharge with Al target. An example of the result is shown in Fig.18, indicating clear absorption lines at 394.40nm and 396.15nm of Al. The experimental absorbance using LED-S-CCD was two orders of magnitude smaller than that using HCL-M-PMT under the same conditions as expected from the theoretical estimation, but absorption limit of 2×10^{-4} could be detected owing to the stable operation of LED and CCD. Fig. 19 shows the discharge power dependence of sputtered Al atom density measured by HCL-M-PMT and LED-S-CCD during magnetron sputtering. Both Al densities agreed well, indicating the Al density was measured with high reliability.

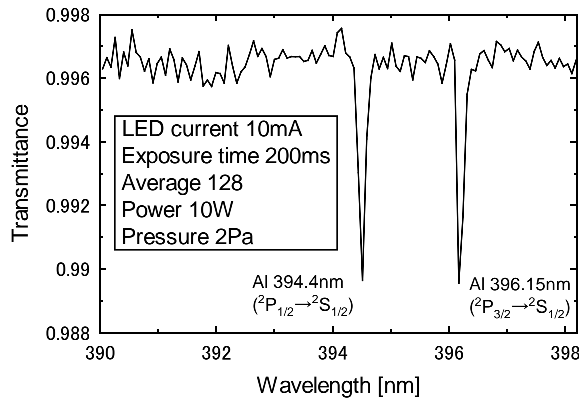

Fig. 18 Absorption spectrum of Al atom measured with LED-S-CCD in a DC planar magnetron discharge.

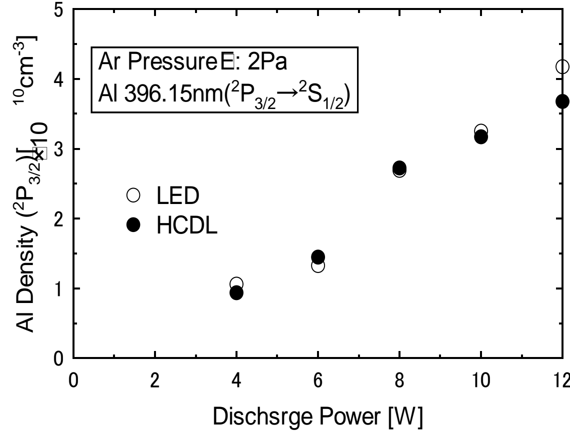

Fig.19 Discharge power dependence of sputtered Al atom density using HCL-M-PMT and LED-S-CCD during magnetron sputtering at 2Pa.

4.3. Measurement of Gas Temperature Using an Extra Cavity Diode Laser Absorption

High resolution diode laser absorption spectroscopy is a powerful tool to diagnose particle density and temperature in plasmas [44, 53]. With the progress in diode laser technology, inexpensive tunable single mode diode lasers with external cavity which are also called as external cavity diode lasers (ECDLs) [54-58] have recently been applied for the measurements of velocity distributions of In [59], He [60], Ar [61], Al [62], and O [63] etc. To grasp the neutral Ar gas temperature in the ICP assisted sputtering, we have measured the distribution functions of metastable Ar by using a home-made ECDL with Littrow configuration. The ECDL was composed of a diode laser (Opnext HL6738MG), a grating (1800 grooves/mm) for rough tuning and a piezo element for fine tuning. The ECDL delivered a single mode output power of ~5 mW at 696.735nm of the metastable Ar absorption transition ($4s^2[3/2]_2^0 \rightarrow 4p^2[1/2]_1$). The wavelength was monitored by a 25 cm spectrometer and the spectral scanning was monitored by a scanning Fabry Perot interferometer (THORLABS SA200-6A). The power of the diode laser beam was attenuated below 10 μW to avoid saturation. The spectral bandwidth of the laser was less than 25 MHz. The laser beam path was set at a position of 3 from the target.

Space average gas temperature (T_{Ar}) and metastable Ar density ($N_{\mathrm{Ar}}{}^{\mathrm{m}}$) were obtained by a curve fitting of the experimental data with the theoretically calculated absorption line profile function taking into

account the saturation of absorption. It is noted that the temperature of metastable Ar ($T_{Ar}{}^{m}$) is the same as that of the ground state Ar (T_{Ar}) because the translational motion is the same in both species. An example of the experimental absorption line profile (obtained at a pressure of 10 mTorr, at a sputtering power of 40 W and ICP RF power of 300 W) is shown in Fig. 20 with a calculated fitting line profile, where T_{Ar} and $N_{Ar}{}^{m}$ were estimated to be 410K and 4.7×10^{10} cm^{-3} respectively. The T_{Ar} was in proportion to ICP RF power, and the the T_{Ar} and $N_{Ar}{}^{m}$ were 320 K and 4.5×10^{9} cm^{-3} respectively for the 10 mTorr Ar ICP without the magnetron discharge. The detection limit of $N_{Ar}{}^{m}$ was about 10^{9} cm^{-3}.

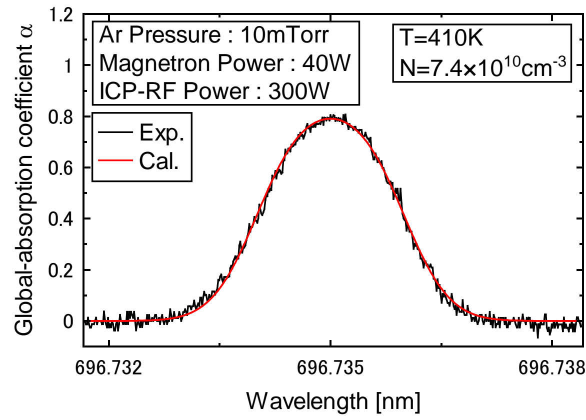

Fig.20 Absorption line profile of the $4s^2[3/2]_2{}^0 \rightarrow 4p^2[1/2]_1$ transition of Ar observed in ICP assisted sputtering at ICP RF power of 300 W, magnetron power of 40 W, at 10 mTorr.

Figure 21 shows the ICP RF power dependence of Ar gas temperature measured by the homemade ECDL using the $4s^2[3/2]_2{}^0 \rightarrow 4p^2[1/2]_1$ transition of metastable Ar at a pressure of 30 mTorr with a magnetron power of 0 W (closed triangle) and 40 W (closed circle). For the 30 mTorr magnetron discharge with the AZO target at a sputtering power of 40 W, T_{Ar} and $N_{Ar}{}^{m}$ were measured to be 440 K and 4×10^{9} cm^{-3}. With superimposing the ICP RF power from 0 to 300 W on the magnetron discharge, T_{Ar} monotonically increased from 440 to 620 K with increasing ICP RF power as shown in Fig. 21; however, $N_{Ar}{}^{m}$ increased from 4×10^{9}cm^{-3} to 8×10^{10}cm^{-3} for increasing ICP RF power from 0 to 100 W then saturated for the further increase in ICP RF power. The increase in T_{Ar} is due to the gas heating effect in high density plasmas [64, 65]. ICP RF power dependence of T_{Ar} for the sole ICP without magnetron

discharge is also shown in Fig. 21 for comparison. We find that T_{Ar} is increased by 80 K with the mixing of sputtered metal atoms. Since the T_{Ar} and N_{Ar}^{m} in the ICP assisted sputter-deposition were considerably larger than those in a conventional planar magnetron discharge, the heat fluxes to the substrate due to neutral Ar atoms in the ICP assisted sputter-deposition were estimated by taking into account thermal accommodation of gases. As a result, the contribution of the ground state Ar atoms to the total heat flux to the substrate was estimated about 10 %, and that of metastable Ar atoms less than 1 %.

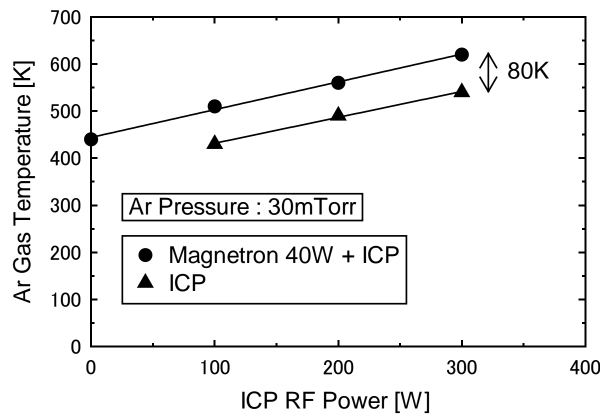

Fig.21 ICP RF power dependence of Ar gas temperature measured by the homemade ECDL using the $4s^2[3/2]_2^0 \rightarrow 4p^2[1/2]_1$ transition of metastable Ar at a pressure of 30 mTorr with the magnetron power of 0 W (closed triangle) and 40 W (closed circle).

As described above, our understanding of the ICP assisted sputter-deposition has been gradually increasing. For the moment, however, the film resistivity of our AZO films deposited with ICP assisted sputter-deposition is several times higher than those obtained with other deposition techniques. However, novel ideas to improve film quality such as the solid-phase crystallization from amorphous phase [66] have been reported. By employing and combining these new ideas with ICP assisted sputtering, we expect to further improve the film conductivity of AZO, as the ionized sputter-deposition has not been fully cultivated.

5. Summary

Inductively coupled plasma (ICP) assisted DC sputter-deposition was used for the deposition of Al-doped ZnO (AZO or ZnO:Al) thin films. With increasing ICP RF power, film properties such as deposition rate, crystallinity, transparency and resistivity were improved. To understand the plasma-surface interaction, several electrical and optical plasma diagnostics were carried out. It was revealed that the high density ICP heated the substrate through a high heat flux to the substrate, resulting in a high quality film deposition without the need for intentional substrate heating. The heat flux to the substrate was predominantly contributed by the plasma ions and electrons, not by the neutral Ar atoms which were also significantly heated up in the ICP. The substrate position where the highest quality films were obtained was found to coincide with the position where the substrate heat flux took the maximum of about 3000 Wm^{-2}.

Acknowledgement

The authors wish to thank T. Iwata, K. Komine, R. Kan, K. Uehara, R. Shindo, H. Kitagawa for their help in the experiment, and Prof. K. Sakai of Miyazaki University for performing the XRD and XPS analyses of AZO films. This research was partially supported by a Grant-in-Aid for Scientific Research (C) from the Japan Society for the Promotion of Science (No. 20540485) in 2008-2010 and by Special Coordination Funds for Promoting Science and Technology sponsored by Japan Science and Technology Agency (JST) in 2009-2011.

References

[1] K.L. Chopra, S. Major, D.K. Pandya, Thin Solid Films **102**, pp.1-46 (1982).

[2] T. Minami, H. Sato, K. Ohashi, T. Tomofuji, S. Takata, Journal of Crystal Growth **117**, pp.370–374 (1992).

[3] K. Ellmer, A. Klein, B. Rech, *Transparent conductive zinc oxide: basics and applications in thin film solar cells* (Springer, Berlin, 2008).

[4] Stephan Lany and Alex Zunger, Phys. Rev. Lett. **98**, 045501 (2007) [4 pages]

[5] Ellmer, R. Mientus, Thin Solid Films **516**, pp.5829–5835 (2008).

[6] B. Szyszka, in *Transparent conductive zinc oxide: basics and applications in thin film solar cells*, ed. K. Ellmer, A. Klein, B. Rech (Springer, Berlin, 2008) pp.187-233.

[7] K. Iwata, T. Sakemi, A. Yamada, P. Fons, K. Awai, T. Yamamoto, M. Matsubara, H. Tampo, S. Niki, Thin Solid Films **445**, pp.274–277 (2003).

[8] K. Yamaya, Y. Yamaki, H. Nakanishi, and S. Chichibu, Appl. Phys. Lett. **72**, pp.235-237 (1998)

[9] Y. H. Han, S. J. Jung, J. J. Lee, J. H. Joo, Surf, Coat. Technol. **174-175**, pp.235-239 (2003).

[10] S. J. Jung, Y. H. Han, B. M. Koo, J. J. Lee, J. H. Joo, Thin Solid Films **475**, pp.275-278 (2005).

[11] S. Iwai, Y. Matsuda, M. Shinohara, and H. Fujiyama, Abstracts and Full-Paper CD of the 18th Int. Symp. on Plasma Chemistry, August 26-31, 2007, Kyoto, Japan, 396 (2007) [4pages].

[12] Y. Matsuda, R. Kan, T. Iwata, K. Komine, K. Uehara, T. Shibasaki, M. Shinohara, Proc. CD of the 19th Int. Sympo. on Plasma Chemistry (ISPC19), edited by A. von Keudell, J. Winter, M. Boke, V. Schulz-von der Gathen, Bochum, Germany, July 26th - 31st, 2009, P.2.2.20 (2009) [4pages].

[13] S Fay and A. Shah, in *Transparent conductive zinc oxide: basics and applications in thin film solar cells*, ed. K. Ellmer, A. Klein, B. Rech (Springer, Berlin, 2008) pp.235-302.

[14] M. Lorentz, in *Transparent conductive zinc oxide: basics and applications in thin film solar cells*, ed. K. Ellmer, A. Klein, B. Rech (Springer, Berlin, 2008) pp.303-357.

[15] A. Kuroyanagi , Jpn. J. Appl. Phys. **28**, pp.219-222 (1989).

[16] A.F. Aktaruzzaman, G.L. Sharma, L.K. Malhotra, Thin Solid Films **198**, pp. 67–74（1991）.

[17] W. Tang, D.C. CameronThin Solid Films **238**, pp.83–87 (1994).

[18] M.Kemell, F. Dartigues, M. Ritala, M. Leskelä, Thin Solid Films **434**, pp.20–23 (2003).

[19] M. Yamashita, Jpn. J. Appl. Phys. **26**, pp.721-727 (1987).

[20] S. M. Rossnagel and J. Hopwood, Appl. Phys. Lett. **63**, pp.3285-3287 (1993).

[21] J. Hopwood, and F. Qian, J. Appl. Phys. **78**, pp.758-765 (1995).

[22] Y. Matsuda, Y. Koyama, K. Tashiro and H. Fujiyama, Thin Solid Films **435**, pp.154-160 (2003).

[23] Y. Matsuda, M. Iwaya, Y. Koyama, M. Shinohara, and H. Fujiyama, Thin Solid Films **457**, pp.64-68 (2004).

[24] Andre Anders, Thin Solid Films **502**, pp.22-28 (2006).

[25] Allen L Garner, Appl. Phys. Lett. **92**, 011505 (2008)[3pages].

[26] S. Iwai, Y. Matsuda, M. Shinohara, and H. Fujiyama, Abstracts and Full-Paper CD of the 18th Int. Symp. on Plasma Chemistry, August 26-31, 2007, Kyoto, Japan (2007) [4pages].

[27] Y. Matsuda, R. Kan, T. Iwata, K. Komine, K. Uehara, T. Shibasaki, M. Shinohara, Proc. CD of the 19th Int. Sympo. on Plasma Chemistry (ISPC19), edited by A. von Keudell, J. Winter, M. Boke, V. Schulz-von der Gathen, Bochum, Germany, July 26th - 31st, 2009, P.2.2.20 (2009) [4pages].

[28] Y. Matsuda, R. Kan, T. Iwata, T. Kitagawa, R. Shindo and M. Shinohara, Abstract Book of the 5th DAE-BRNS National Sympo. on Pulsed Laser Deposition of Thin Films and Nanostructured Materials (PLD-2009), December 2-4, 2009, IIT Madras, Chennai India, IRT11, p.27 (2009),

[29] Y. Matsuda, R. Shindo, A. Hirashima, M. Shinohara, *Inductively Coupled Plasma Assisted Sputter-Deposition of Al-doped ZnO Thin Films*, Bulletin of the American Physical Society, 63rd Annual Gaseous Electronics Conf. and 7th Int. Conf. on Reactive Plasmas, October 4-8, 2010, Paris France, Volume **55**, Number 7, DTP.00036 (2010) [2pages].

[30] Y. Matsuda, A. Hirashima, K. Mine, T. Hashimoto, D. Matsuoka, and M. Shinohara, and T. Okada, *Deposition of Transparent Conductive Aluminum-Doped ZnO Films Using RF Superposed DC Sputtering*, Joint IIT Madras-Japan symp. on ZnO nano-crystals and related materials, January 8-10 2012, IIT-Madras Madras India (2012) [1page].

[31] R. Dsa, K. Adhikary, and S. Ray: Jpn. J. of Appl. Phys. **47** (3), pp.1501–1506 (2008).

[32] H. Kersten, G. M. W. Kroesen, R. Hippler, Thin Solid Films **332**, pp.282-289 (1998).

[33] H. Kersten, D. Rohde, J. Berndt, H. Deutsch, R. Hippler, Thin Solid Films **377-378**, pp.585-591 (2000).

[34] H. Kersten, E. Stoffels, W. W. Stoffels, M. Otte, C. Csambal, H. Deutsch, R. Hippler, J. Appl. Phys. **87**, pp.3637-3645 (2000).

[35] H. Kersten, H. Deutsch, H. Steffen, G.M.W. Kroesen, R. Hippler, Vacuum **63**, pp.385-431 (2001).

[36] A.L. Thomann, N. Semmar, R. Dussrt, and J. Mathias, Rev. of Sci. Instrum. **77**, 033501 (2006).

[37] R.Dussart,A.L.Thomann: Appl.Phys. **93**, 131502 (2008).

[38] R. Wendt and K. Ellmer, K. Wiesemann, J. Appl. Phys. **82**, pp.2115- 2122 (1997).

[39] L. Sirghi, G. Popa, Y. Hatanaka, Thin Solid Films **515**, pp.1334-1339 (2006).

[40] H. Matsuura, T. Jida, Contrib. Plasma Phys. **46**, pp.406-410 (2006).

[41] Y. Matsuda, H. Kitagawa, K. Mine, M. Shinohara, Bulletin of the American Physical Society, 63rd Annual Gaseous Electronics Conf. and 7th Int. Conf. on Reactive Plasmas, October 4-8, 2010, Paris France, Volume **55**, Number 7, CTP.00010 (2010)[2pages].

[42] H. Kitagawa, R. Kan, K. Mine, M. Shinohara, Y. Matsuda, TENCON 2010 IEEE Region 10 Conf., November 21-24 2010, Fukuoka Japan. T2-5.P2, pp. 2208-2212 (ISBN: 978-1-4244-6888-1) (2010).

[43] H. Kitagawa, K. Mine, M. Shinohara, Y. Matsuda, T. Okada, Proc. of the 20th Int. Sympo. on Plasma Chemistry (ISPC20), Philadelphia USA, July 24-29 2011, FDM56, ID537, (2011) [4pages].

[44] Vladimir N. Ochkin, *Spectroscopy of Low Temperature Plasma* (Wiley-VCH, Germany, 2009).

[45] A. Kono, S. Takashima, M. Hori and T. Goto, J. of Nucl. Mater. **76**, pp.460-464 (2000).

[46] E. Castanos-Martinez, M. Moisan, Spectrochimica Acta Part B **65**, 199-209 (2010).

[47] T. Iwata, R. Shindo, M. Shinohara, Y. Matsuda, Proc. of 31st Int. Sympo. on Dry Process, Busan Exhibition & Convention Center, Busan, Korea, September 24 to 25, 2009, 5-P11, pp.151-152 (2009).

[48] T. Iwata, R. Sindo, K. Komine, M. Shinohara, Y. Matsuda, Proceedings CD of the 27th Sympo. on Plasma Processing, Kaiyo Kinen Kaikan, Yokohama, February 1-3, 2010, P1-15, pp.157-158 (2010).

[49] R. Shindo, T. Iwata, A. Hirashima, M. Shinohara, Y. Matsuda, TENCON 2010 IEEE Region 10 Conf., November 21-24 2010, Fukuoka Japan. T2-7.3 pp.1002-1006 (ISBN: 978-1-4244-6888-1) (2010).

[50] G. Cunge, D. Vempaire, M. Touzeau, and N. Sadeghi, Appl. Phys. Lett. **91**, 231503 (2007)[3pages]

[51] R. Shindo, A. Hirashima, M. Shinohara, Y. Matsuda, K. Sakai, T. Okada, Proc of the 20th Int. Sympo. on Plasma Chemistry (ISPC20), Philadelphia USA, July 24-29 2011, FDM55, ID536, (2011)[4pages].

[52] G.V.Samsonov, "The Oxide Hand book" chapter II, (IFI/PLENUM, New York 1973)

[53] K Tachibana, H Harima and Y Urano, J. Phys. B: At. Mol. Phys. **15**, 3169 (1982).

[54] K. B. MacAdam, A. Steinbach, and C. Wieman, Am. J. Phys. **60** (12) (1992) pp.1098-1111.

[55] D, Wandt, M. Laschek, K. Przyklenk, A. Tunnermann, H. Welling, Opt. Com. **130**, pp.81-84 (1996).

[56] S. Eriksson, A. E .M. Lindberg, B. Stahlberg, Optics & Laser Technology **31**, pp.473-477 (1999).

[57] X. M. Zhang, A. Q. Liu, C. Lu, and D. Y. Tang, J. Quantum Electronics **41** (2), pp.187-197 (2005).

[58] B. Mroziewicz, Opto-Electronics Review, **16**-4, pp.347-366 (2008).

[59] L. Hildebrandt, R. Knispel, S. Stry, J. R. Sacher, and F. Schael, Appl. Opt. **42** (12), pp.2110-2118 (2003).

[60] R. F. Boivina, E. E. Scime, Rev. Sci. Instrum. **74**, pp.4352-4361 (2003).

[61] A. Bol'shakov, B. A. Cruden, Technical Physics **53** (11), pp.1423-1432 (2008).

[62] M. Wolter, H. T. Do, H. Steffen, R. Hippler, J. Phys. D: Appl. Phys. **38**, pp.2390–2395 (2005).

[63] K. Sasaki, Y. Okumura, and R. Asaoka, Int. J. of Spectroscopy **10**.1155, 627571 (2010).

[64] M. W. Kiehlbauch and D. B. Graves, Appl. Phys. **91**, pp.3539-3546 (2002).

[65] D. B. Hash, D. Bose, M. V. V. S. Rao, B. A. Cruden, M. Meyyappan, S. P. Sharma, J. of Appl. Phys. **90** (5), pp.2148-2157 (2001).

[66] N. Itagaki, K. Kuwahara, K. Nakahara, D. Yamashita, G. Uchida, K. Koga, and M. Shiratani, Applied Physics Express **4**, 011101 (2011)[2pages].